

SAS-Net: Scene-Appearance Separation Network for Robust Spatiotemporal Registration in Bidirectional Photoacoustic Microscopy

Jiahao Qin*

* Corresponding author: jiahao.qin19@gmail.com

Abstract. High-speed optical-resolution photoacoustic microscopy (OR-PAM) with bidirectional scanning enables rapid functional brain imaging but introduces severe spatiotemporal misalignment from coupled scan-direction-dependent domain shift and geometric distortion. Conventional registration methods rely on brightness constancy, an assumption violated under bidirectional scanning, leading to unreliable alignment. A unified scene-appearance separation framework is proposed to jointly address domain shift and spatial misalignment. The proposed architecture separates domain-invariant scene content from domain-specific appearance characteristics, enabling cross-domain reconstruction with geometric preservation. A scene consistency loss promotes geometric correspondence in the latent space, linking domain shift correction with spatial registration within a single framework. For *in vivo* mouse brain vasculature imaging, the proposed method achieves normalized cross-correlation (NCC) of 0.961 ± 0.038 and structural similarity index (SSIM) of 0.894 ± 0.021 , substantially outperforming conventional methods. Ablation studies demonstrate that domain alignment loss is critical, with its removal causing 82% NCC reduction (0.961 to 0.175), while scene consistency and cycle consistency losses provide complementary regularization for optimal performance. The method achieves 11.2 ms inference time per frame (89 fps), substantially exceeding typical OR-PAM acquisition rates and enabling real-time processing. These results suggest that the proposed framework enables robust high-speed bidirectional OR-PAM for reliable quantitative and longitudinal functional imaging. The code will be publicly available at <https://github.com/D-ST-Sword/SAS-Net>.

Keywords: Photoacoustic microscopy · Image registration · Domain shift · Scene-appearance separation

1 Introduction

Photoacoustic microscopy (PAM) has emerged as a powerful imaging modality that combines cellular-level spatial resolution with functional imaging capability. OR-PAM exploits the photoacoustic effect, whereby pulsed laser excitation generates ultrasonic waves through thermoelastic expansion. This enables label-free visualization of endogenous chromophores, including hemoglobin, melanin, and

lipids, with microscopic resolution [5, 29, 34, 35]. Owing to these unique advantages, OR-PAM has been widely used to study cerebral hemodynamics, tumor angiogenesis, and metabolic activity in living tissues [17, 18, 38], where high temporal resolution is often required to capture dynamic physiological processes.

To meet this demand, voice-coil-based OR-PAM systems have been developed to enable high-speed bidirectional raster scanning [6, 36], nearly doubling the imaging speed compared with unidirectional scanning. However, forward and backward acquisitions often exhibit scan-direction-dependent artifacts, resulting in severe spatiotemporal misalignment that compromises quantitative analysis and longitudinal studies. These artifacts arise at both intra-frame and inter-frame levels.

Intra-frame artifacts. These arise from discrepancies between forward and backward scanning lines within a frame, originating from two sources: (1) geometric misalignment, caused by mechanical hysteresis and actuator dynamics during high-speed bidirectional motion, leading to systematic spatial offsets [22, 27]; and (2) domain shift, where scan-direction-dependent differences in effective sampling (*e.g.*, timing offsets and velocity asymmetry) and system response produce systematic intensity differences between forward and backward acquisitions. Importantly, these two effects are intrinsically coupled: scan-direction-dependent domain shift fundamentally violates brightness constancy [4, 8], making conventional image registration methods unreliable for estimating geometric misalignment.

Inter-frame artifacts. These arise from temporal variations in imaging conditions across the entire longitudinal image sequence. Factors such as physiological motion, temperature-induced scanner drift, and sample deformation introduce frame-to-frame geometric misalignment, complicating quantitative time-series analysis of functional dynamics.

Current solutions to bidirectional scanning artifacts primarily rely on conventional image registration methods [11, 20, 31, 33], including feature-based and deformable registration approaches. These methods attempt to directly align forward and backward acquisitions using intensity-based correspondence estimation. However, such approaches inherently assume brightness constancy between source and target images—an assumption that is fundamentally violated by scan-direction-dependent domain shift in bidirectional scanning.

As demonstrated in experiments, traditional registration methods, including SIFT, Demons, and optical flow, exhibit limited effectiveness under these conditions, resulting in low structural similarity after alignment. The core challenge is the coupling between domain shift and geometric misalignment: scan-direction-dependent intensity variations hinder reliable correspondence estimation, while inaccurate geometric alignment further exacerbates appearance discrepancies. Consequently, neither factor can be effectively addressed in isolation.

To address these challenges, we propose SAS-Net (Scene-Appearance Separation Network), a unified framework based on principled scene-appearance separation for robust spatiotemporal registration in bidirectional optical-resolution

photoacoustic microscopy. The core insight of SAS-Net is that scene information, corresponding to the underlying anatomical structure, can be separated from appearance variations induced by scan-direction-dependent imaging conditions. This separation enables joint correction of domain shift and geometric misalignment within a single end-to-end trainable network.

The main contributions of this work are listed as follows:

1. We propose a scene-appearance separation framework that jointly addresses domain shift and spatial registration in bidirectional OR-PAM by disentangling domain-invariant structure from acquisition-specific appearance.
2. We introduce a scene consistency loss that enforces geometric correspondence in latent space, enabling implicit inter-frame alignment without explicit frame-to-frame registration.
3. We validate the proposed method on *in vivo* mouse brain vasculature data, achieving state-of-the-art performance with real-time processing capability (89 fps). The code will be publicly available.

2 Related Work

2.1 Photoacoustic Microscopy and Bidirectional Scanning

Photoacoustic microscopy has rapidly evolved as a powerful modality for *in vivo* imaging [34]. Early OR-PAM systems achieved micrometer-scale spatial resolution but were limited by slow scanning speed, the capture of fast physiological dynamics [5, 35]. The development of high-speed scanning mechanisms, such as voice-coil actuators [6] and rotational scanning strategies including polygon and rotary scanners [19, 26, 29, 40], substantially improved temporal resolution, enabling functional imaging of rapid hemodynamic processes.

To further increase imaging speed, bidirectional scanning has been widely adopted [17]. Existing solutions to the resulting artifacts largely rely on post-hoc calibration-based corrections [22, 27] or manual phase adjustment, which are time-consuming and often insufficient under dynamic *in vivo* conditions. Recently, deep learning-based methods have shown promise for PAM image enhancement [7, 21, 25, 30], but bidirectional artifact correction remains constrained by the limited availability of paired ground truth data for training.

2.2 Deformable Image Registration

Medical image registration aims to establish spatial correspondence for anatomical comparison and motion correction [4, 24, 28]. Classical approaches include intensity-based methods such as mutual information [23] and diffeomorphic algorithms like Demons [31] and SyN [1]. Deep learning methods such as Voxel-Morph [2] enable fast registration by predicting deformation fields, with extensions incorporating attention mechanisms [3] and robustness to contrast variations [9]. Despite these advances, existing registration methods implicitly rely on the assumption that the images to be registered share globally comparable

intensity distributions. When systematic domain shift is present, as in bidirectional scanning, this assumption is violated, leading to unreliable correspondence estimation and registration failure.

2.3 Unpaired Image-to-Image Translation

Generative adversarial networks (GANs) have enabled unpaired image translation without requiring pixel-wise correspondence. Pix2Pix [13] demonstrated conditional image generation using paired data, while CycleGAN [39] extended this to unpaired settings through cycle consistency. Subsequent works such as MUNIT [12] and DRIT [15] further disentangle domain-invariant content from domain-specific appearance, enabling flexible cross-domain synthesis. Despite their effectiveness in modeling appearance variations, these methods are not designed to enforce precise spatial alignment. In particular, cycle consistency encourages content preservation at a global level but does not guarantee local geometric consistency, allowing subtle spatial distortions that can accumulate in fine anatomical structures, such as micro-vasculature.

2.4 Joint Registration and Translation

Recent studies have explored the intersection of image registration and domain shift correction. For example, SynthMorph [9] trains registration networks on synthetically generated images with diverse contrasts to improve robustness to intensity variations, while diffusion models have also been investigated for joint generation and registration tasks [14]. However, these approaches rely primarily on data augmentation and may not adequately capture the scan-direction-dependent domain shift inherent in bidirectional scanning system. In contrast, the proposed method models scene-appearance separation under geometric constraints, directly addressing the intrinsic coupling between domain shift and spatial misalignment in bidirectional OR-PAM imaging.

3 Method

A unified framework is presented for bidirectional OR-PAM image registration based on scene-appearance separation. The proposed method jointly corrects domain shift and geometric misalignment within a single end-to-end trainable network. The overall architecture is illustrated in Fig. 1.

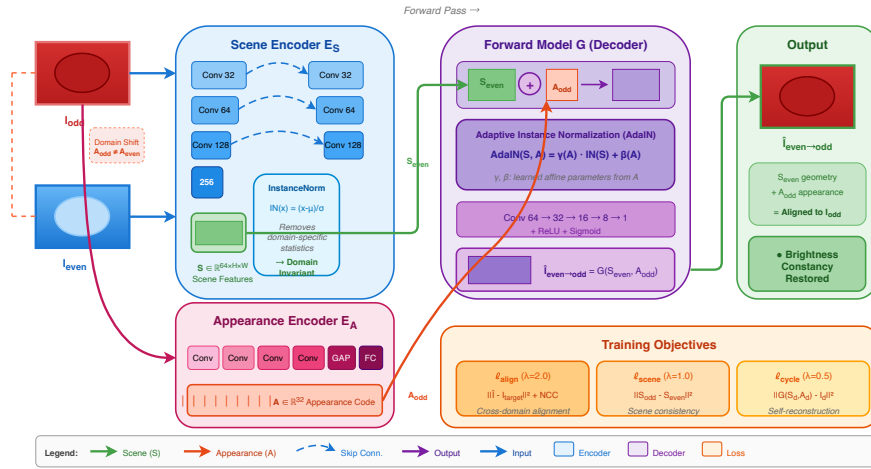


Fig. 1: Overview of our scene-appearance separation framework. **(a)** Model architecture and registration results: Scene Encoder E_S extracts domain-invariant anatomical structure using instance normalization; Appearance Encoder E_A captures domain-specific acquisition parameters via global average pooling; Forward Model G synthesizes images using feature modulation layers. The scene consistency loss $\mathcal{L}_{\text{scene}}$ ensures geometric alignment between S_{odd} and S_{even} . Left and right panels show before/after registration comparison with odd-even overlay visualization demonstrating effective column alignment. **(b)** Implicit inter-frame alignment through shared scene space: Our unified approach maps all frames to a shared scene space where $S_1 \approx S_2 \approx \dots \approx S_n$ (domain-invariant). The shared Scene Encoder with InstanceNorm removes domain statistics, and the Forward Model re-renders structures with target acquisition parameters, producing domain-aligned outputs ready for registration without explicit inter-frame registration.

3.1 Problem Formulation: A Forward Modeling Perspective

A forward modeling perspective is adopted, motivated by the underlying physics of OR-PAM image formation. In bidirectional OR-PAM, the observed image I is determined by two independent factors: (1) the underlying anatomical structure S , and (2) the acquisition parameters A , which encompass scan-direction-dependent imaging characteristics such as effective sampling conditions, intensity response, and system gain. The imaging process can be expressed as:

$$I = \mathcal{F}(S, A) + \epsilon, \quad (1)$$

where \mathcal{F} denotes the physical image formation process and ϵ represents noise. Let \mathcal{D}_{odd} and $\mathcal{D}_{\text{even}}$ denote the odd-line (forward) and even-line (backward) scanning domains, respectively. Both domains observe the same underlying structure S but under different acquisition parameters:

$$I_{\text{odd}} = \mathcal{F}(S, A_{\text{odd}}) + \epsilon_{\text{odd}}, \quad I_{\text{even}} = \mathcal{F}(S, A_{\text{even}}) + \epsilon_{\text{even}}. \quad (2)$$

This formulation highlights a key challenge in bidirectional OR-PAM: direct image registration is unreliable because the two images differ not only geometrically but also in acquisition conditions ($A_{\text{odd}} \neq A_{\text{even}}$). Instead, we decompose the problem into two complementary tasks. The inverse problem aims to infer the domain-invariant structure S and domain-specific acquisition parameters A from the observed image I :

$$(S, A) = \mathcal{F}^{-1}(I). \quad (3)$$

While the forward problem corresponds to re-synthesizing an image by rendering the inferred structure under target acquisition conditions accordingly:

$$I_{\text{even} \rightarrow \text{odd}} = \mathcal{F}(S_{\text{even}}, A_{\text{odd}}) \approx I_{\text{odd}}. \quad (4)$$

From this perspective, cross-domain registration is equivalent to re-rendering: the shared structure is first extracted from the source domain and then rendered under the target domain's acquisition conditions. Conventional registration methods fail because they implicitly assume $I_{\text{odd}} \approx T(I_{\text{even}})$ for some spatial transformation T , neglecting the fundamental domain shift induced by differing acquisition parameters.

3.2 Network Architecture: Implementing the Forward Model

The proposed framework implements the forward model (Eq. (1)) through three neural network modules: a Scene Encoder extracting structure S , an Appearance Encoder extracting acquisition parameters A , and a Forward Model G synthesizing images by recombining these two representations.

Scene Encoder E_S . The Scene Encoder addresses the inverse problem of extracting domain-invariant anatomical structure from observed images. We adopt a U-Net architecture with instance normalization (IN) [32] as the key design choice. From a physical perspective, instance normalization removes channel-wise mean μ and standard deviation σ , which encodes domain-specific intensity characteristics:

$$\text{IN}(x) = \frac{x - \mu(x)}{\sigma(x)}. \quad (5)$$

By normalizing these statistics, the encoder is encouraged to retain domain-invariant structural information shared across scanning directions. The network adopts an encoder–bottleneck–decoder architecture with skip connections:

$$S = E_S(I) \in \mathbb{R}^{C_S \times H \times W}, \quad (6)$$

where $C_S = 64$ denotes the dimensionality of the structure feature. Skip connections preserve fine vascular details critical for accurate registration.

Appearance Encoder E_A . The Appearance Encoder extracts compact acquisition parameter codes that capture domain-specific characteristics, inspired by compact signal encoding in bioengineering systems [16]. It consists of a lightweight convolutional network followed by global average pooling:

$$A = E_A(I) \in \mathbb{R}^{C_A}, \quad (7)$$

where $C_A = 32$ denotes the acquisition code dimension. From a physical perspective, the acquisition parameters A encode scan-direction–dependent imaging responses. Global average pooling removes spatial information, ensuring that A captures scene-agnostic acquisition characteristics that affect the image globally rather than at specific spatial locations.

Forward Model G . The Forward Model implements the forward imaging equation $I = \mathcal{F}(S, A)$ as a learnable neural network. We introduce an Imaging Response Modulator that applies domain-specific intensity characteristics to domain-invariant structure through feature modulation:

$$\text{Modulate}(S, A) = \gamma(A) \odot \text{IN}(S) + \beta(A), \quad (8)$$

where $\gamma(A), \beta(A) \in \mathbb{R}^{C_S}$ are learned affine parameters (scale and shift) linearly derived from the acquisition code. From a physical perspective, the Imaging Response Modulator applies domain-specific intensity characteristics to domain-invariant structure representing the underlying biological anatomy. Mathematically, this operation can be interpreted as a transport of feature statistics in latent space, where the normalized feature distribution, characterized by (μ, σ) , is mapped to the target domain-specific distribution. The parameters $\gamma(A)$ model the contrast and gain response, while $\beta(A)$ controls the intensity offset. The final synthesis can be shown as:

$$\hat{I} = G(S, A). \quad (9)$$

Cross-Domain Reconstruction as Re-Rendering. Cross-domain reconstruction follows a forward modeling perspective. Given images I_{odd} and I_{even} from two scanning domains, structure and acquisition parameters are first extracted:

$$\begin{aligned} S_{\text{odd}} &= E_S(I_{\text{odd}}), & A_{\text{odd}} &= E_A(I_{\text{odd}}), \\ S_{\text{even}} &= E_S(I_{\text{even}}), & A_{\text{even}} &= E_A(I_{\text{even}}). \end{aligned} \quad (10)$$

The forward problem can be solved through bidirectional cross-domain reconstruction:

$$I_{\text{even} \rightarrow \text{odd}} = G(S_{\text{even}}, A_{\text{odd}}), \quad I_{\text{odd} \rightarrow \text{even}} = G(S_{\text{odd}}, A_{\text{even}}). \quad (11)$$

From a physical perspective, cross-domain registration can be interpreted as a re-rendering process. The output $I_{\text{even} \rightarrow \text{odd}}$ represents the anatomical structure extracted from the even-line image rendered under the odd-line domain's imaging characteristics. Unlike conventional registration, which directly warps pixel intensities, the proposed approach preserves geometric structure while transforming only the imaging response.

Implicit Inter-Frame Alignment via Shared Structure Space. A key property of the proposed framework is that it achieves implicit inter-frame alignment without explicit frame-to-frame registration. This property arises from the shared structure representation enforced by cross-domain reconstruction of the entire temporal sequence. While the primary registration output is obtained using S_{even} and A_{odd} , the cross-domain reconstruction $I_{\text{odd} \rightarrow \text{even}} = G(S_{\text{odd}}, A_{\text{even}})$ enforces consistency of the scene representations extracted by the Scene Encoder across domains. For cross-domain reconstruction to be successful (*i.e.*, $I_{\text{odd} \rightarrow \text{even}} \approx I_{\text{even}}$), the network must satisfy:

$$G(S_{\text{odd}}, A_{\text{even}}) \approx I_{\text{even}} = G(S_{\text{even}}, A_{\text{even}}). \quad (12)$$

Because the same acquisition parameters A_{even} and the same forward model G are used, this condition implies that the structure representations extracted from forward and backward scans must be consistent in the latent structure space:

$$S_{\text{odd}} \approx S_{\text{even}} \quad (\text{in structure space}). \quad (13)$$

As a result, the Scene Encoder is encouraged to learn domain-invariant representations that capture only the underlying anatomical structure. This formulation further extends to multiple frames. Since the Scene Encoder E_S is shared across all frames during training, the same structure consistency constraint naturally extends across time. For frames observing the same anatomy, the extracted structure representations satisfy:

$$S_{(1)} \approx S_{(2)} \approx \dots \approx S_{(n)} \quad (14)$$

for frames observing the same anatomy. Consequently, all frames are implicitly mapped to a shared structure space, enabling both intra-frame alignment (between forward and backward scans) and inter-frame alignment (across the image sequence) without explicit frame-to-frame registration.

3.3 Loss Functions

The network is trained using a composite objective function designed to ensure reconstruction fidelity, cycle consistency, domain alignment, and geometric preservation across frames. Collectively, these loss terms jointly enforce the implicit inter-frame alignment detailed in Sec. 3.2.

Scene Consistency Loss. The proposed scene consistency loss plays a central role in enabling implicit inter-frame alignment by enforcing geometric consistency between structures extracted from different scanning domains within a domain-invariant feature space:

$$\mathcal{L}_{\text{scene}} = \|S_{\text{odd}} - S_{\text{even}}\|_2^2 + \lambda_{\text{cos}}(1 - \cos(S_{\text{odd}}, S_{\text{even}})) \quad (15)$$

where $\|\cdot\|_2^2$ denotes mean squared error, and the cosine similarity is computed by first flattening the spatial dimensions:

$$\cos(S_{\text{o}}, S_{\text{e}}) = \frac{\text{vec}(S_{\text{o}})^\top \text{vec}(S_{\text{e}})}{\|\text{vec}(S_{\text{o}})\|_2 \|\text{vec}(S_{\text{e}})\|_2} \quad (16)$$

where $S_{\text{o}} = S_{\text{odd}}$ and $S_{\text{e}} = S_{\text{even}}$ for brevity, with $\text{vec}(\cdot)$ denoting vectorization. We set $\lambda_{\text{cos}} = 0.1$. This loss directly bridges domain shift correction and registration: by forcing the scene representations to match, we ensure that the underlying geometry is preserved during domain transfer.

Cycle Consistency Loss. Self-reconstruction ensures the encoder-decoder preserves information:

$$\begin{aligned} \mathcal{L}_{\text{cycle}} = & \|G(S_{\text{odd}}, A_{\text{odd}}) - I_{\text{odd}}\|_2^2 + \|G(S_{\text{even}}, A_{\text{even}}) - I_{\text{even}}\|_2^2 \\ & + \lambda_{\text{ssim}}(2 - \text{SSIM}_{\text{odd}} - \text{SSIM}_{\text{even}}) \end{aligned} \quad (17)$$

where $\text{SSIM}_{\text{odd}} = \text{SSIM}(G(S_{\text{odd}}, A_{\text{odd}}), I_{\text{odd}})$ and $\text{SSIM}_{\text{even}} = \text{SSIM}(G(S_{\text{even}}, A_{\text{even}}), I_{\text{even}})$, with $\lambda_{\text{ssim}} = 0.5$.

Domain Alignment Loss. The primary registration objective ensures the translated image $I_{\text{even} \rightarrow \text{odd}}$ aligns with I_{odd} :

$$\begin{aligned} \mathcal{L}_{\text{align}} = & \|I_{\text{even} \rightarrow \text{odd}} - I_{\text{odd}}\|_2^2 + \lambda_{\text{ncc}}(1 - \text{NCC}(I_{\text{even} \rightarrow \text{odd}}, I_{\text{odd}})) \\ & + \lambda_{\text{grad}} \mathcal{L}_{\text{grad}} \end{aligned} \quad (18)$$

where NCC denotes normalized cross-correlation, and $\mathcal{L}_{\text{grad}}$ is a gradient matching loss promoting structural alignment:

$$\mathcal{L}_{\text{grad}} = \|\nabla_x I_{\text{even} \rightarrow \text{odd}} - \nabla_x I_{\text{odd}}\|_1 + \|\nabla_y I_{\text{even} \rightarrow \text{odd}} - \nabla_y I_{\text{odd}}\|_1 \quad (19)$$

with $\lambda_{\text{ncc}} = 0.5$ and $\lambda_{\text{grad}} = 0.3$.

Total Loss. The complete training loss is:

$$\mathcal{L}_{\text{total}} = \lambda_{\text{scene}} \mathcal{L}_{\text{scene}} + \lambda_{\text{cycle}} \mathcal{L}_{\text{cycle}} + \lambda_{\text{align}} \mathcal{L}_{\text{align}} \quad (20)$$

with weights $\lambda_{\text{scene}} = 1.0$, $\lambda_{\text{cycle}} = 0.5$, $\lambda_{\text{align}} = 2.0$. Note that domain alignment receives the highest weight as it directly measures registration quality.

4 Experiments

4.1 Experimental Setup

Dataset. We evaluate the proposed method on the OR-PAM-Reg-4K benchmark dataset, acquired using a custom-built high-speed bidirectional OR-PAM system based on voice-coil motor scanning. The system operates at a B-scan rate of 40 Hz, enabling rapid imaging of cerebral microvasculature through cranial windows with high spatial and temporal resolution. The OR-PAM-Reg-4K dataset comprises 4,248 image pairs at 512×256 resolution, extracted from high-resolution frames of three mice. The dataset is split into training (80%, 3,396 samples), validation (10%, 420 samples), and test (10%, 432 samples) sets at the frame level to ensure no spatial overlap between splits. To support reproducibility and benchmarking, the OR-PAM-Reg-4K dataset is publicly available [37].

Implementation Details. Scene Encoder uses 32 base channels with 3 down-sampling levels, while the Appearance Encoder uses 16 base channels with global average pooling. The Forward Model mirrors the Scene Encoder with feature modulation at each level, resulting in a total of 3.5M parameters. The network is trained for 200 epochs using Adam optimizer (learning rate 10^{-4} , $\beta_1 = 0.5$, $\beta_2 = 0.999$) with a batch size of 4. All experiments are conducted on NVIDIA RTX 4090 GPU with data augmentation including random flips, rotations ($\pm 10^\circ$), and intensity scaling (0.9–1.1 \times).

4.2 Intra-frame Registration Results

Tab. 1 summarizes the quantitative results for intra-frame bidirectional artifact correction. Registration performance is evaluated using the Structural Similarity Index (SSIM) and Normalized Cross-Correlation (NCC) between odd columns and their corresponding registered even columns. Fig. 2 provides a qualitative comparison, and Fig. 3 shows quantitative distributions across three mice. The main observations are summarized below.

Table 1: Quantitative Comparison of Registration Methods on OR-PAM-Reg-4K Test Set. SSIM, PSNR, and NCC measure alignment quality between odd and registered even columns. Best results in **bold**, second best underlined.

Method	SSIM \uparrow	PSNR \uparrow	NCC \uparrow
<i>Traditional Methods</i>			
Original (Unregistered)	0.482	19.46	0.167
SIFT [20]	<u>0.679</u>	<u>24.14</u>	0.723
Demons [33]	0.579	20.35	0.323
Optical Flow [11]	0.455	18.99	0.061
SyN (ANTs) [1]	0.613	21.55	0.411
<i>Deep Learning Methods</i>			
VoxelMorph [2]	0.659	22.88	<u>0.724</u>
TransMorph [3]	0.641	21.09	0.594
SAS-Net (Ours)	0.894 ± 0.021	32.50 ± 1.6	0.961 ± 0.038

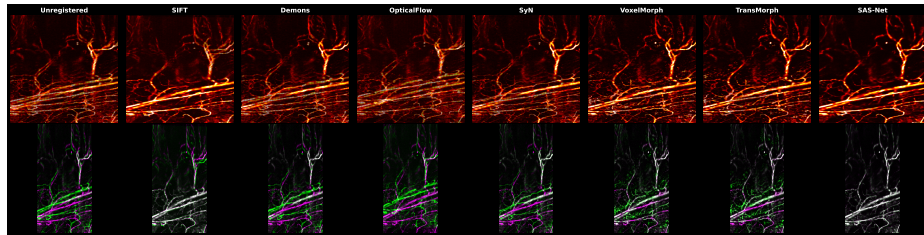


Fig. 2: Qualitative comparison of registration results. Visual comparison on a representative frame across all eight methods. For each method: interleaved images with HOT colormap, odd-even overlay (odd in magenta, even in green, alignment as white), and grayscale visualization. Cross-frame overlay (rightmost) shows inter-frame alignment quality. Our method achieves continuous vascular structures with minimal color separation in overlays.

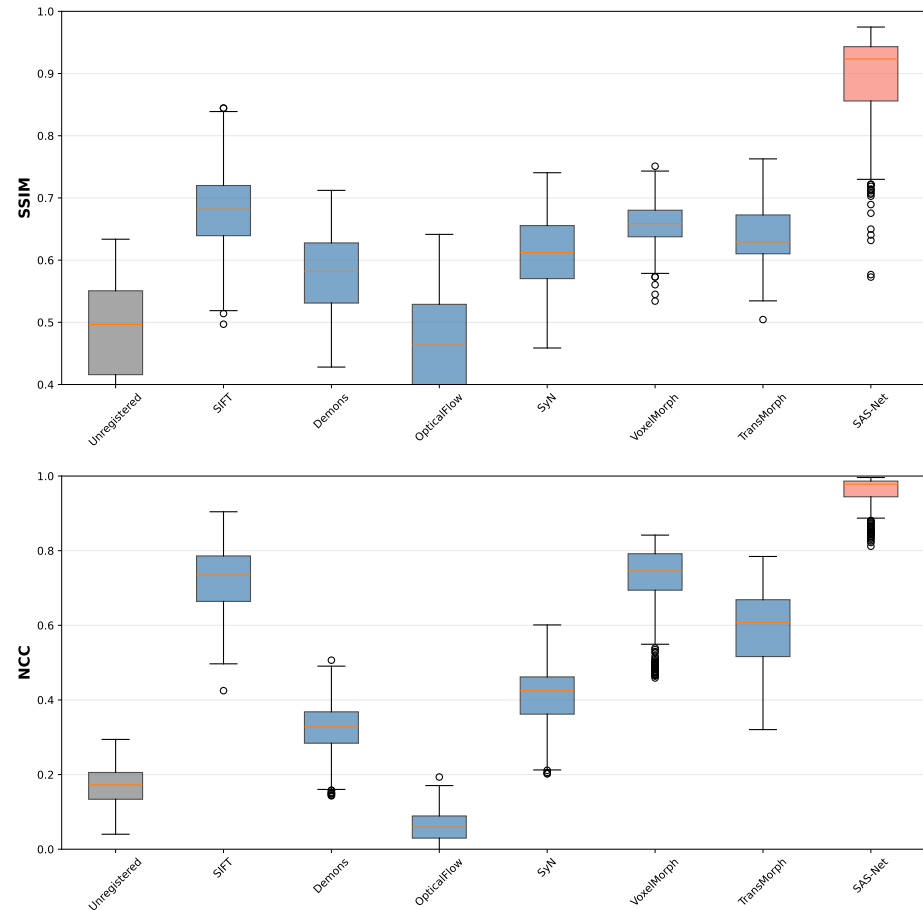


Fig. 3: Quantitative comparison on OR-PAM-Reg-4K test set. SSIM (top) and NCC (bottom) box plots showing metric distributions across 432 test samples. SAS-Net consistently outperforms all baseline methods.

Performance of conventional registration methods. Conventional baselines show moderate improvement under bidirectional scanning but remain substantially limited. Among traditional methods, SIFT achieves the highest SSIM of 0.679, followed by SyN (0.613), Demons (0.579), and Optical Flow (0.455), compared with 0.482 for the unregistered baseline. Optical Flow performs worse than some alternatives, indicating that dense flow estimation struggles under severe domain shift. Overall, these results indicate that registration methods relying on brightness constancy cannot fully address the domain shift induced by bidirectional scanning.

Performance of the proposed method. The proposed scene–appearance separation framework substantially improves registration accuracy, achieving an SSIM of 0.894 ± 0.021 and an NCC of 0.961 ± 0.038 . This corresponds to absolute improvements of 0.412 in SSIM and 0.794 in NCC relative to the unregistered baseline. Compared to the best traditional method (SIFT), SAS-Net achieves 31.7% higher SSIM (0.894 vs 0.679) and 32.9% higher NCC (0.961 vs 0.723). Consistent improvements are observed across all evaluated frames, indicating robust performance under scan-direction–dependent intensity variations.

Effect of joint domain shift correction and registration. Unlike conventional methods that assume brightness constancy, the proposed approach explicitly models scan-direction–dependent domain shift through scene–appearance separation. This joint treatment enables reliable registration under forward–backward intensity differences.

4.3 Inter-frame Temporal Consistency

The proposed framework achieves implicit inter-frame alignment through a shared scene space (Sec. 3.2). The proposed method attains an average inter-frame NCC of 0.964 ± 0.010 across 117 consecutive frame pairs, with stable performance across the entire sequence. Such temporal stability is critical for longitudinal and functional imaging studies.

4.4 Ablation Study

Tab. 2 presents a systematic ablation analysis of individual loss components and architectural choices. Experiments are conducted on the OR-PAM-Reg-4K benchmark with 512×256 resolution images, trained for 40 epochs. Performance is evaluated using SSIM, PSNR, and NCC between odd columns and registered even columns.

The domain alignment loss $\mathcal{L}_{\text{align}}$ is the most critical component: its removal causes NCC to drop from 0.961 to 0.175 (82% reduction), demonstrating that direct supervision of cross-domain reconstruction is essential. Removing $\mathcal{L}_{\text{cycle}}$ or $\mathcal{L}_{\text{scene}}$ causes moderate decreases (NCC: 0.955 and 0.953, respectively), confirming that cycle consistency stabilizes training while scene consistency enforces geometric correspondence in latent space. Removing the appearance encoder E_A

Table 2: Ablation Study on Loss Components and Architecture. Experiments conducted on OR-PAM-Reg-4K benchmark (512×256 resolution, 40 epochs). Best results in **bold**.

Configuration	SSIM \uparrow	PSNR \uparrow	NCC \uparrow
SAS-Net (Full)	0.894 ± 0.021	32.50 ± 1.6	0.961 ± 0.038
w/o $\mathcal{L}_{\text{scene}}$	0.867 ± 0.022	31.63 ± 1.5	0.953 ± 0.036
w/o $\mathcal{L}_{\text{cycle}}$	0.871 ± 0.020	31.87 ± 1.5	0.955 ± 0.035
w/o $\mathcal{L}_{\text{align}}$	0.569 ± 0.107	21.1 ± 3.4	0.175 ± 0.050
w/o E_A (Appearance Encoder)	0.851 ± 0.022	30.53 ± 1.6	0.944 ± 0.039

reduces SSIM from 0.894 to 0.851, indicating that explicit appearance encoding is important for domain disentanglement. The full model achieves the best overall performance, demonstrating synergistic contributions from all components.

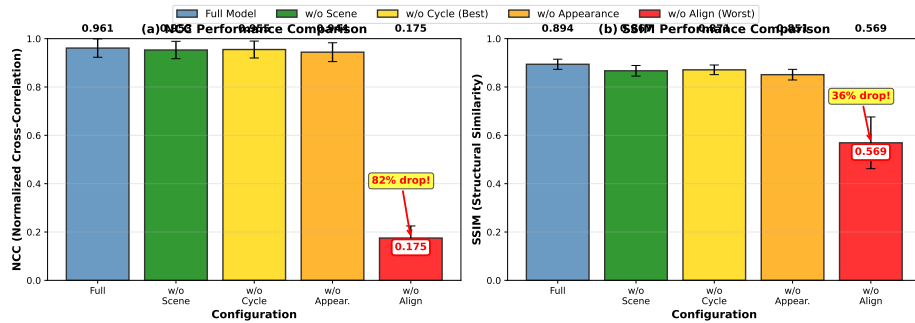


Fig. 4: Ablation study results on OR-PAM-Reg-4K test set. (a) NCC and (b) SSIM performance across different configurations. Removing alignment loss causes catastrophic 82% NCC drop. All other components contribute positively, with the full model achieving the best overall performance. Error bars show standard deviation across 432 test samples.

4.5 Vascular Continuity Analysis

Vascular Continuity Index (VCI) is introduced as a domain-specific metric measuring the continuity of vascular structures across odd-even column boundaries. Specifically, we merge odd and even columns into an interleaved image and compute the Sobel gradient in the horizontal direction. Three representative ROIs are selected for evaluation as shown in Fig. 5. The VCI is computed as:

$$\text{VCI} = 1 - \frac{1}{\tau_{\max}} \cdot \frac{\sum_{j \in \mathcal{B}} \sum_i e_{ij} \cdot \mathbf{1}[v_{ij} > \tau]}{\sum_{i,j} \mathbf{1}[v_{ij} > \tau]} \quad (21)$$

where \mathcal{B} denotes odd-even column boundaries (positions 1, 3, 5, …), e_{ij} is the Sobel edge response at position (i, j) , v_{ij} is the merged image intensity, $\mathbf{1}[\cdot]$ is the indicator function, $\tau = 0.05$ is the vessel detection threshold, and $\tau_{\max} = 0.3$ is an empirical normalization constant.

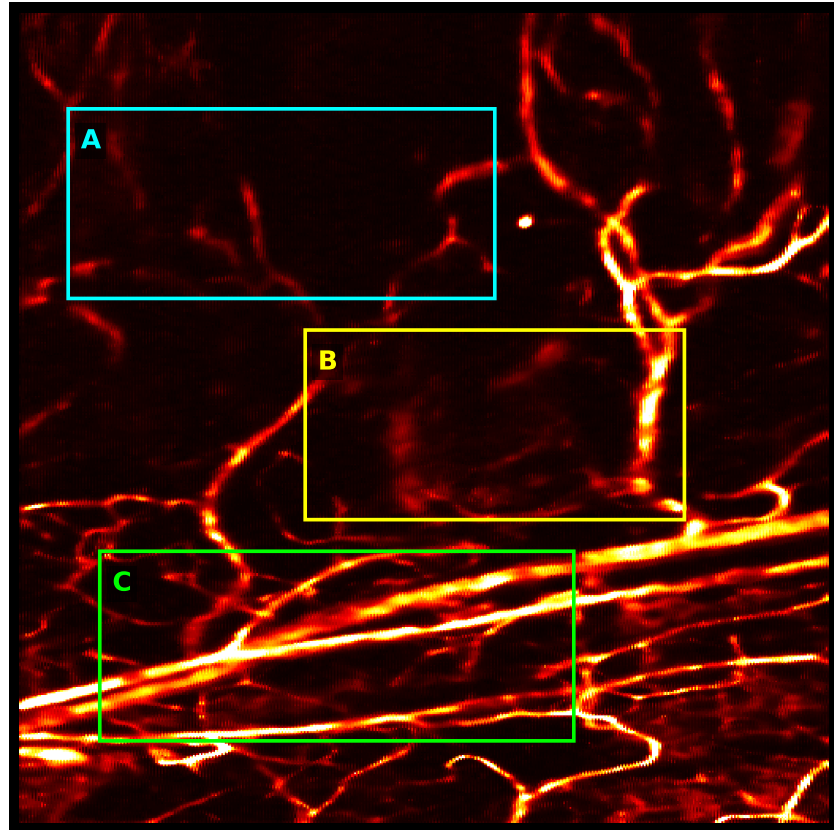


Fig. 5: ROI selection for qualitative analysis. Three representative regions (A, B, C) are selected from the interleaved image to evaluate registration quality across different vascular structures.

Fig. 6 presents detailed ROI analysis across all methods. SAS-Net achieves substantially improved visual alignment at vessel boundaries compared to all baselines, which show visible discontinuities at vessel edges.

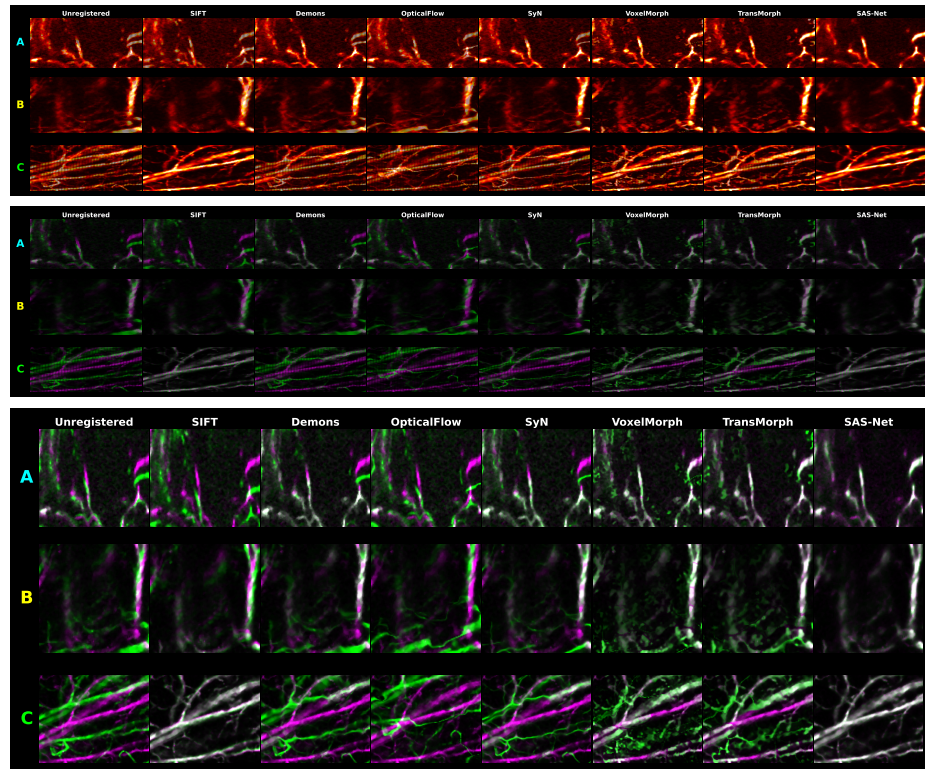


Fig. 6: Detailed ROI comparison across all eight methods for regions A, B, and C (*cf.* Fig. 5). Top: interleaved odd-even view with HOT colormap. Middle: odd columns in magenta and even columns in green. Bottom: pixel-level overlay (white indicates alignment). SAS-Net achieves visually superior alignment compared to all baselines.

4.6 Computational Efficiency

Tab. 3 compares computational requirements across methods. All inference times are measured on NVIDIA RTX 4090 GPU, averaged over 100 runs.

Table 3: Computational Efficiency Comparison. Inference times (ms) measured on NVIDIA RTX 4090 GPU for 512×256 column pairs.

	Traditional Methods				Deep Learning Methods		
	SyN	Demons	SIFT	Opt. Flow	VoxelMorph	TransMorph	SAS-Net
Time (ms)	3439.5	113.4	35.5	15.4	1.7	6.3	11.2

While VoxelMorph (1.7 ms) and TransMorph (6.3 ms) are faster, they fail to achieve satisfactory registration quality due to unaddressed domain shift. SyN requires 3.4 seconds per frame, making it impractical for real-time use. SAS-Net achieves an optimal trade-off at 11.2 ms (89 fps), suitable for dynamic imaging.

5 Discussion

Why forward modeling succeeds. The effectiveness of the proposed framework rests on two insights. First, formulating registration as re-rendering through a differentiable forward model $I = \mathcal{F}(S, A)$ explicitly decouples domain shift from geometric alignment. Conventional methods seek a spatial transformation T such that $I_{\text{odd}} \approx T(I_{\text{even}})$, which is ill-posed when $A_{\text{odd}} \neq A_{\text{even}}$. Our approach instead identifies the underlying structure S and synthesizes it under target acquisition parameters, bypassing the brightness constancy constraint. Second, the shared Scene Encoder creates a common structure space where all frames are automatically aligned (Sec. 3.2), eliminating the need for separate inter-frame registration. Compared with the two-stage approach of Hong *et al.* [10], which cascades intra-frame and inter-frame U-Net registration in pixel space, the proposed unified framework avoids error accumulation and explicitly models domain shift through scene-appearance separation.

Clinical implications. The vascular continuity analysis (Sec. 4.5) shows that our method improves VCI from 0.370 (unregistered) to 0.857 (2.3 \times enhancement), specifically improving alignment at vessel boundaries where discontinuities most impact blood flow velocity estimation [18], vessel diameter measurement, and functional connectivity analysis.

Limitations. Two failure modes were identified: severe illumination inhomogeneity ($>50\%$ across the field of view) may cause the Appearance Encoder to capture spatially-varying patterns ($\sim 5\%$ of frames), and sparse vascular regions may yield inconsistent scene features. The unsupervised paradigm and

domain-agnostic architecture (instance normalization, feature modulation) suggest broader applicability to other raster-scanning modalities. Future work includes cross-cohort validation, extension to volumetric 3D reconstruction, and hardware-level optimization for resource-constrained deployment.

6 Conclusion

This study presents SAS-Net, a unified scene-appearance registration framework for bidirectional OR-PAM imaging. Through comprehensive experiments on the OR-PAM-Reg-4K benchmark (432 test samples), SAS-Net achieves NCC of 0.961 ± 0.038 and SSIM of 0.894 ± 0.021 , outperforming traditional methods by 32.9% in NCC and 31.7% in SSIM, establishing a new state-of-the-art for OR-PAM registration. By isolating domain-invariant structure from acquisition-specific appearance, the proposed method reformulates registration as re-rendering within a shared latent space, bypassing the brightness constancy assumption that limits conventional approaches. Ablation studies confirm that domain alignment loss is the critical component (82% NCC drop when removed), while appearance disentanglement provides essential domain separation. The framework generalizes to imaging modalities with coupled domain shifts and spatial misalignments.

Acknowledgements

This work was supported in part by the National Natural Science Foundation of China under Grant 62305066, in part by the Joint Fund of Ministry of Education for Equipment Pre-research under Grant 8091B03012310, in part by the Shanghai Pujiang Program under Grant 23PJ1401600, in part by the Shanghai Municipal Health Commission of Science and Research Fund under Grant 20234Y0234, and in part by the Shanghai Municipal Education Commission Project under Grant 24RGZNB01. All animal procedures were performed in compliance with institutional guidelines and were reviewed and approved by the Committee on the Ethics of Animal Experiments at Fudan University Shanghai Medical College (Permit No. 20230301-103).

References

1. Avants, B.B., Epstein, C.L., Grossman, M., Gee, J.C.: Symmetric diffeomorphic image registration with cross-correlation: Evaluating automated labeling of elderly and neurodegenerative brain. *Med. Image Anal.* **12**(1), 26–41 (Feb 2008) [3](#), [11](#)
2. Balakrishnan, G., Zhao, A., Sabuncu, M.R., Guttag, J., Dalca, A.V.: VoxelMorph: A learning framework for deformable medical image registration. *IEEE Trans. Med. Imaging* **38**(8), 1788–1800 (Aug 2019) [3](#), [11](#)
3. Chen, J., Frey, E.C., He, Y., Segars, W.P., Li, Y., Du, Y.: TransMorph: Transformer for unsupervised medical image registration. *Med. Image Anal.* **82**, 102615 (Nov 2022) [3](#), [11](#)

4. Chen, J., Liu, Y., Wei, S., Bian, Z., Subramanian, S., Carass, A., Prince, J.L., Du, Y.: A survey on deep learning in medical image registration: New technologies, uncertainty, evaluation metrics, and beyond. *Med. Image Anal.* **100**, 103385 (Feb 2025) [2](#), [3](#)
5. Cho, S., Kim, M., Ahn, J., Kim, Y., Lim, J., Park, J., Kim, H.H., Kim, W.J., Kim, C.: An ultrasensitive and broadband transparent ultrasound transducer for ultrasound and photoacoustic imaging in-vivo. *Nat. Commun.* **15**(1), 1444 (Feb 2024) [2](#), [3](#)
6. Cikaluk, B.D., Restall, B.S., Haven, N.J.M., Martell, M.T., McAlister, E.A., Zemp, R.J.: Rapid ultraviolet photoacoustic remote sensing microscopy using voice-coil stage scanning. *Opt. Express* **31**(6), 10136–10149 (Mar 2023) [2](#), [3](#)
7. Gröhl, J., Schellenberg, M., Dreber, K., Maier-Hein, L.: Deep learning for biomedical photoacoustic imaging: A review. *Neural Netw.* **185**, 107181 (May 2025). <https://doi.org/10.1016/j.neunet.2025.107181> [3](#)
8. Hering, A., Hansen, L., Mok, T.C., Chung, A.C., Siebert, H., Häger, S., Lange, A., Kuckertz, S., Heldmann, S., Shao, W., et al.: Learn2Reg: Comprehensive multi-task medical image registration challenge, dataset and evaluation in the era of deep learning. *IEEE Trans. Med. Imaging* **42**(3), 697–712 (2023) [2](#)
9. Hoffmann, M., Billot, B., Greve, D.N., Iglesias, J.E., Fischl, B., Dalca, A.V.: SynthMorph: Learning contrast-invariant registration without acquired images. *IEEE Trans. Med. Imaging* **41**(3), 543–558 (Mar 2022) [3](#), [4](#)
10. Hong, X., Tang, F., Wang, L., Chen, J.: Unsupervised deep learning enables real-time image registration of fast-scanning optical-resolution photoacoustic microscopy. *Photoacoustics* **38**, 100632 (Aug 2024) [17](#)
11. Horn, B.K., Schunck, B.G.: Determining optical flow. *Artif. Intell.* **17**(1-3), 185–203 (Aug 1981) [2](#), [11](#)
12. Huang, X., Liu, M.Y., Belongie, S., Kautz, J.: Multimodal unsupervised image-to-image translation. In: Proc. Eur. Conf. Comput. Vis. (ECCV). pp. 179–196. Springer (Sep 2018) [4](#)
13. Isola, P., Zhu, J.Y., Zhou, T., Efros, A.A.: Image-to-image translation with conditional adversarial networks. In: Proc. IEEE Conf. Comput. Vis. Pattern Recognit. (CVPR). pp. 5967–5976 (Jul 2017) [4](#)
14. Kazerouni, A., Aghdam, E.K., Heidari, M., Azad, R., Fayyaz, M., Hacihamiloglu, I., Merhof, D.: Diffusion models in medical imaging: A comprehensive survey. *Med. Image Anal.* **88**, 102846 (Aug 2023) [4](#)
15. Lee, H.Y., Tseng, H.Y., Huang, J.B., Singh, M., Yang, M.H.: Diverse image-to-image translation via disentangled representations. In: Proc. Eur. Conf. Comput. Vis. (ECCV). pp. 36–52. Springer (Sep 2018) [4](#)
16. Li, W., Cao, Y., Wang, C., Sepúlveda, N.: Ferroelectret nanogenerators for the development of bioengineering systems. *Cell Rep. Phys. Sci.* **4**(5), 101388 (May 2023). <https://doi.org/10.1016/j.xcrp.2023.101388> [7](#)
17. Liu, C., Chen, J., Zhang, Y., Zhu, J., Wang, L.: Five-wavelength optical-resolution photoacoustic microscopy of blood and lymphatic vessels. *Adv. Photon.* **3**(1), 016002 (Jan 2021) [2](#), [3](#)
18. Liu, C., Liang, Y., Wang, L.: Single-shot photoacoustic microscopy of hemoglobin concentration, oxygen saturation, and blood flow in sub-microseconds. *Photoacoustics* **17**, 100156 (Mar 2020) [2](#), [17](#)
19. Liu, L., Xu, Z., Lai, Z., Xu, B., Wu, T., Ma, G., Zhang, H., Li, J., Ma, W., Lei, T., Li, X., Guo, Z., Song, Z., Chen, N., Ye, S., Meng, J., Lai, P., Shen, F., Chang, J., Zhu, Y., Zheng, H., Zheng, W., Liu, C.: Photoacoustic and fluorescence hybrid

- microscope for cortex-wide imaging of neurovascular dynamics with subcellular resolution. *Sci. Adv.* **11**(30), eadw5275 (Jul 2025) [3](#)
20. Lowe, D.G.: Distinctive image features from scale-invariant keypoints. *Int. J. Comput. Vis.* **60**(2), 91–110 (Nov 2004) [2, 11](#)
 21. Ma, H., Ren, S., Wei, X., Yu, Y., Qian, J., Chen, Q., Zuo, C.: Enhanced photoacoustic microscopy with physics-embedded degeneration learning. *Opto-Electron. Adv.* **8**(3), 240189 (Mar 2025) [3](#)
 22. Maraghechi, S., Hoefnagels, J.P.M., Peerlings, R.H.J., Geers, M.G.D.: Correction of scan line shift artifacts in scanning electron microscopy: An extended digital image correlation framework. *Ultramicroscopy* **187**, 144–163 (Apr 2018) [2, 3](#)
 23. Mattes, D., Haynor, D.R., Vesselle, H., Lewellyn, T.K., Eubank, W.: PET-CT image registration in the chest using free-form deformations. *IEEE Trans. Med. Imaging* **22**(1), 120–128 (Jan 2003) [3](#)
 24. Oliveira, F.P.M., Tavares, J.M.R.S.: Medical image registration: A review. *Comput. Methods Biomed. Eng.* **17**(2), 73–93 (Jan 2014) [3](#)
 25. Park, E., Misra, S., Hwang, D.G., Yoon, C., Ahn, J., Kim, D., Jang, J., Kim, C.: Unsupervised inter-domain transformation for virtually stained high-resolution mid-infrared photoacoustic microscopy using explainable deep learning. *Nat. Commun.* **15**(1), 10892 (Dec 2024) [3](#)
 26. Qin, W., Li, T., Li, L., Jin, T., Li, B., Qi, W., Chen, Y., Li, H., Ruan, S., Guo, H., Liang, X., Xi, L.: A cortex-wide multimodal microscope for simultaneous Ca²⁺ and hemodynamic imaging in awake mice. *Nat. Commun.* **16**(1), 9364 (Oct 2025) [3](#)
 27. Shintate, R., Ishii, T., Ahn, J., Kim, J.Y., Kim, C., Saito, Y.: High-speed optical resolution photoacoustic microscopy with MEMS scanner using a novel and simple distortion correction method. *Sci. Rep.* **12**(1), 9221 (June 2022) [2, 3](#)
 28. Sotiras, A., Davatzikos, C., Paragios, N.: Deformable medical image registration: A survey. *IEEE Trans. Med. Imaging* **32**(7), 1153–1190 (July 2013) [3](#)
 29. Taboada, C., Delia, J., Chen, M., Ma, C., Peng, X., Zhu, X., Jiang, L., Vu, T., Zhou, Q., Yao, J., O'Connell, L., Johnsen, S.: Glassfrogs conceal blood in their liver to maintain transparency. *Science* **378**(6626), 1315–1320 (Dec 2022). <https://doi.org/10.1126/science.abl6620> [2, 3](#)
 30. Tang, X., Chen, J., Qu, Z., Zhu, J., Amjad, M., Yang, M., Wan, Y., Wang, L.: High sensitivity photoacoustic imaging by learning from noisy data. *IEEE Transactions on Medical Imaging* **44**(7), 2868–2877 (July 2025). <https://doi.org/10.1109/TMI.2025.3552692> [3](#)
 31. Thirion, J.P.: Image matching as a diffusion process: An analogy with Maxwell's demons. *Med. Image Anal.* **2**(3), 243–260 (Sept 1998) [2, 3](#)
 32. Ulyanov, D., Vedaldi, A., Lempitsky, V.S.: Instance normalization: The missing ingredient for fast stylization. *arXiv preprint arXiv:1607.08022* (Jul 2016) [7](#)
 33. Vercauteren, T., Pennec, X., Perchant, A., Ayache, N.: Diffeomorphic demons: Efficient non-parametric image registration. *NeuroImage* **45**(1), S61–S72 (Mar 2009) [2, 11](#)
 34. Wang, L.V., Hu, S.: Photoacoustic tomography: In vivo imaging from organelles to organs. *Science* **335**(6075), 1458–1462 (Mar 2012) [2, 3](#)
 35. Yang, F., Wang, Z., Shi, W., Wang, M., Ma, R., Zhang, W., Li, X., Wang, E., Xie, W., Zhang, Z., Shen, Q., Zhou, F., Yang, S.: Advancing insights into in vivo meningeal lymphatic vessels with stereoscopic wide-field photoacoustic microscopy. *Light Sci. Appl.* **13**(1), 96 (Apr 2024) [2, 3](#)

36. Yao, J., Wang, L., Yang, J.M., Maslov, K.I., Wong, T.T.W., Li, L., Huang, C.H., Zou, J., Wang, L.V.: High-speed label-free functional photoacoustic microscopy of mouse brain in action. *Nat. Methods* **12**(5), 407–410 (May 2015) [2](#)
37. Zhang, T., Yan, C., Lan, X.: OR-PAM-Reg-4K: A benchmark dataset for bidirectional OR-PAM registration (2026). <https://doi.org/10.57967/hf/7721>, <https://huggingface.co/datasets/chengliuyan/OR-PAM-Reg-4K> [10](#)
38. Zhang, Y., Chen, J., Zhang, J., Zhu, J., Liu, C., Sun, H., Wang, L.: Super-low-dose functional and molecular photoacoustic microscopy. *Adv. Sci.* **10**(23), e2302486 (Aug 2023) [2](#)
39. Zhu, J.Y., Park, T., Isola, P., Efros, A.A.: Unpaired image-to-image translation using cycle-consistent adversarial networks. In: Proc. IEEE Int. Conf. Comput. Vis. (ICCV). pp. 2242–2251 (Oct 2017) [4](#)
40. Zhu, X., Huang, Q., Jiang, L., Nguyen, V.T., Vu, T., Devlin, G., Shaima, J., Wang, X., Chen, Y., Ma, L., Xiang, K., Wang, E., Rong, Q., Zhou, Q., Kang, Y., Asokan, A., Feng, L., Hsu, S.W.D., Shen, X., Yao, J.: Longitudinal intravital imaging of mouse placenta. *Sci. Adv.* **10**(12), eadk1278 (Mar 2024) [3](#)